Appl. Phys. B (2017) 123:142
DOI 10.1007/s00340-017-6714-y

Applied Physics B
Lasers and Optics

Coherent frequency combs for spectroscopy across the 3–5 μm region

Daniel L. Maser[1,2] · Gabriel Ycas[1] · William I. Depetri[3] · Flavio C. Cruz[1,3] · Scott A. Diddams[1,2]

Received: 21 January 2017 / Accepted: 29 March 2017

Abstract A tunable mid-infrared frequency comb was created via difference frequency generation. Pulses between 1 and 1.5 μm were mixed to generate light ranging from 2.6 to 5.2 μm. Two such combs were heterodyned at 5 μm to show their coherence and potential for spectroscopy. The properties of the comb were modeled using numerical simulation, which confirmed the observed bandwidths.

1 Introduction and overview

Mid-infrared (MIR) laser sources are a powerful tool to study the spectroscopic "fingerprints" of various compounds important for many applications [1], including time-resolved spectroscopy [2, 3], radiocarbon detection [4], trace gas sensing [5], and airborne spectroscopy [6, 7]. Traditionally, MIR laser sources have been based on continuous wave (CW) gas and diode lasers [8–10], but more recently there has been significant growth of both optical parametric oscillators (OPOs) [11–14] and quantum cascade lasers (QCLs) [15–19].

In this paper, we employ difference frequency generation (DFG) of portions of the broad spectrum of a near-infrared frequency comb to reach the MIR [20–23]. The strengths of this approach are simplicity and flexibility. It leverages the robust and technologically mature erbium-doped-fiber oscillators at 1.5 μm [24, 25] and takes advantage of non-resonant MIR generation in a single pass through a nonlinear crystal. Additionally, because the MIR light is generated by nonlinear differencing of portions of the near-infrared spectrum, the offset frequency f_0 of the original comb is removed, such that the MIR comb has frequencies which are uniquely determined as harmonics of the near-infrared comb repetition rate, i.e., $\nu_n = nf_{\mathrm{rep}}$. This significantly simplifies the frequency stabilization and yields a frequency comb possessing a unique combination of broad bandwidth spectral coverage, high resolution and absolute frequency information. We note that CW laser-assisted spectroscopy in the MIR has been implemented with a near-infrared comb to also remove the necessity for f_0 stabilization [26].

In the near-infrared, frequency comb spectroscopy has already proved useful in industrial [27] and medical [28] applications, as well as atmospheric greenhouse gas sensing [29]. The spectroscopic technique implemented here is dual-comb spectroscopy, which is an effective means to make rapid, high-bandwidth, well-resolved, and accurate measurements [30, 31]. Dual-comb spectroscopy has been previously explored in the MIR, but at shorter wavelengths [32–37] and with systems that employ OPOs [14, 38] or fully stabilized near-IR combs combined with CW lasers [39]. Here, we instead focus on a straight forward and broad bandwidth dual-comb implementation, with the MIR frequency combs (spanning 2.6–5.2 μm) based on the DFG of two wavelengths of a near-infrared comb laser. While mid-infrared combs have been developed via a similar technique in this spectral region previously [20, 40–50], our work aims to characterize the coherence and noise properties of these mid-infrared sources and optimize the

✉ Scott A. Diddams
scott.diddams@nist.gov

[1] National Institute of Standards and Technology, Boulder, CO 80305, USA

[2] Department of Physics, University of Colorado Boulder, Boulder, CO 80309, USA

[3] Instituto de Fisica Gleb Wataghin, Universidade Estadual de Campinas, Campinas, SP 13083859, Brazil

Published online: 18 April 2017

sources to enable their future implementation in precision dual-comb mid-infrared spectroscopy.

The method of spectral generation described here centers around a robust 1.5-μm erbium fiber oscillator. Through nonlinear broadening in silica fiber [51], the 1.5-μm mode-locked laser can generate spectra ranging from 1 to 2 μm (see Fig. 1, at left). The difference frequency generation between portions of the spectrum around 1 μm and some of the original 1.5-μm light then occurs in a single pass through millimeter-lengths of periodically poled lithium niobate (PPLN) [52]. By tuning the period of the PPLN crystal, we generate spectra spanning from 2.6 to 5.2 μm, limited by the PPLN transparency at long wavelengths [53]. Across this range, single tuning bandwidths of 1–7 THz are achieved, as determined by a combination of phase-matching and input spectral bandwidth. Additionally, for our specific choice of parameters, average powers ranging from 100 μW to 20 mW are generated. The residual intensity noise is characterized to be sufficiently low such that high signal-to-noise ratio (SNR) interferograms can be achieved in the heterodyne between two such combs, thus demonstrating their utility for dual-comb spectroscopy.

2 Theory

Difference frequency generation (DFG) has been well-described in the literature [54–57]. Here we present a brief overview of the theory behind the modeling that we show in Sect. 4.4. Our goal in doing so is to present a simple model that allows us to gain insight into and to compare with the main features observed in the experimental data. In particular, we focus on the physical and experimental parameters of the DFG process that constrain the achievable power and bandwidth.

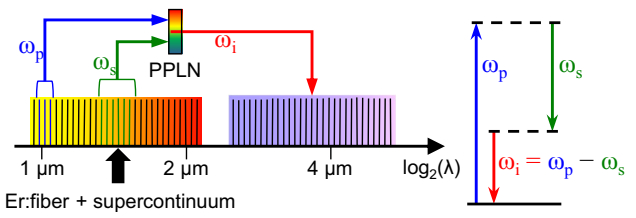

Fig. 1 *Left* Overview of mid-infrared difference frequency generation using a 1.5-μm erbium fiber laser. A supercontinuum was generated and was centered about the 1.5-μm source, portions of which were used in difference frequency generation in periodically poled lithium niobate (PPLN). The details of this procedure are described in Sect. 3.1. *Right* Energy-level diagram of the difference frequency generation process. Pump photons (ω_p) at 1 μm drive the down-conversion process, which is seeded by 1.5-μm signal photons (ω_s), leading to parametric gain in the signal and also generating idler photons (ω_i)

The process of DFG is a three-wave mixing nonlinear process between pump (p), signal (s) and idler (i) waves, also conveniently understood in the photon energy picture of Fig. 1 (at right). In the time domain, DFG can be described by three coupled differential equations [55]:

$$\frac{\partial A_s}{\partial z} = -\sum_{m=1}^{\infty} \frac{(-i)^{m-1}}{m!} k^{(m)} \frac{\partial^m A_s}{\partial t^m} - i\frac{\chi^{(2)}\omega_s}{2n_s c} A_p A_i^* e^{-i\Delta k\cdot z},$$

$$\frac{\partial A_i}{\partial z} = -\sum_{m=1}^{\infty} \frac{(-i)^{m-1}}{m!} k^{(m)} \frac{\partial^m A_i}{\partial t^m} - i\frac{\chi^{(2)}\omega_i}{2n_i c} A_p A_s^* e^{-i\Delta k\cdot z},$$

and

$$\frac{\partial A_p}{\partial z} = -\sum_{m=1}^{\infty} \frac{(-i)^{m-1}}{m!} k^{(m)} \frac{\partial^m A_p}{\partial t^m} - i\frac{\chi^{(2)}\omega_p}{2n_p c} A_s A_i e^{i\Delta k\cdot z},$$

where $A = A(t)$ and $A^*(t)$ are the electric field amplitudes of each wave (signal, idler, pump) in the time-domain and their complex conjugates, $k^{(m)}$ is the mth order dispersion coefficient, $\chi^{(2)}$ is the second-order nonlinearity of the nonlinear medium (in this case, PPLN), ω is the angular frequency of each wave, n is the refractive index of each wave, and $\Delta k = k_p - k_s - k_i - \frac{2\pi}{\Lambda}$ is the magnitude of the wavevector mismatch, where Λ is the poling period of the PPLN crystal. For these simulations, only $m = 1$ and 2 were used; that is, only first- and second-order dispersion were incorporated. The amplitudes of the input fields A_p and A_s were created using measured values of average power, pulse duration, and beam waists. These simulations assumed plane waves with no diffraction, which is valid when the crystal length is within the confocal parameter of the focused beam (accurate for both the 1-and 3-mm crystal lengths used here), and the electric field amplitudes $A(t)$ assumed Gaussian envelopes. The simulations also incorporated PPLN material absorption [53], not shown in the above equations. These coupled equations were then numerically integrated through the PPLN crystal along the z-axis. The results of these simulations were used to confirm observed bandwidth and power measurements, discussed later in Sect. 4.4.

The dynamics of the pulse propagation in the PPLN crystal are dictated by the optical nonlinear interaction among the pulses and their dispersion through the crystal. For a pump beam centered at 1074 nm, the group velocity of the signal pulse at 1.3 μm is 1 % higher than the pump, while the idler group velocity at 5 μm is 4.4 % smaller. For the input pulse durations used in the simulations (400 fs for pump and 60 fs for signal), the group velocity mismatch (GVM) length for pump and signal is 4.65 mm, meaning that they propagate overlapped within each crystal, with the signal leading the pump pulse. As the pump and signal propagate, the continuously generated idler propagates with smaller group velocities for longer wavelengths. For 5-μm pulses and sufficiently longer crystals, the idler leaves a long tail behind the

pump and signal, which can make this pulse much longer and spectrally narrower.

3 Experiment

3.1 Setup

The near-infrared frequency combs used in generating the two mid-infrared combs were modified from those described in [33] to allow for tunability from 2.6 to 5.2 μm. Each frequency comb was based on an erbium fiber ring oscillator, which generated a 1.5-μm frequency comb at 100 MHz (see Fig. 2). One of the oscillators is a MenloSystems C-comb, and the other is based on the design described in Ref. [58]. The generated comb light of each was split into two branches, which produced the pump and signal used in DFG. Most of the fiber-based portions of the systems were made from polarization-maintaining (PM) components, which contributed to the long-term stability.

In the pump branch, a normal-dispersion (nLight LIEKKI Er80-8/125) erbium-doped fiber amplifier (EDFA) (top, in Fig. 2) was used to generate short pulses with high peak power (roughly 200 mW and 70 fs) at 1.5 μm. The fiber lengths in the Menlo oscillator system were 12 cm of PANDA (after 20 cm of internal fiber from the Menlo comb had been removed), 82 cm of PM EDF, and 39 cm of PANDA, and the fiber lengths in the home-built system were 82 cm of PANDA, 94 cm of PM EDF, and 63 cm of PANDA. The generated pulse was launched into a short length (8 cm in the Menlo-based system, 15 cm in home-built oscillator system) of PM highly nonlinear fiber (HNLF) with a zero dispersion wavelength (ZDW) of roughly 1350 nm to create a low-noise dispersive wave at 1 μm [59, 60]. This was the seed for a high-power ytterbium-doped fiber amplifier (YDFA), which produced 2 W at 1 μm and was the pump source in DFG. Both systems stretched the pulses using either fiber Bragg gratings or negative third-order dispersion fibers to roughly 50 ps before launching into either highly doped double-clad ytterbium gain fiber (Nufern PLMA-YDF-10/125-HI-8) or a commercial high-power ytterbium amplifier (Keopsys CYFA-PB-BW1-PM-33-NL1-OM1-M305-FA-FA). The pump pulse was compressed using a pair of transmission diffraction gratings (1600 grooves/mm, not shown in the figure). The pump power that reached the crystal after compression and beam-shaping optics was 735 mW.

The signal branch (bottom, in Fig. 2) also featured an EDFA with similar characteristics to that described previously. The fiber lengths in the Menlo-based system were 60 cm of PANDA, 68 cm of PM EDF, and 48 cm of PANDA, and the fiber lengths in the home-built oscillator system were 132 cm of PANDA, 102 cm of PM EDF, and 60 cm of PANDA. The output of this amplifier was launched into a short section of PM HNLF (7 cm of PM HNLF in the Menlo-based system, 3.5 cm in the home-built oscillator system) with a ZDW of roughly 1520 nm; the pulses' chirp and peak power were catered towards generating spectral power between 1.3 and 1.5 μm (see Fig. 4 and description in Sect. 3.2). This was the signal source in DFG. The total signal power across the entire spectrum was 81, 6 mW of which is in the 1.3-μm phase-matching bandwidth for 5-μm production.

Focusing both beams to the same position with similar waists and confocal parameters is important for strong mode overlap, and thus idler generation. The PM HNLF used in the signal branch has a small core, and we used a collimator with a high numerical aperture to collect and collimate the most light. This beam was minimally shaped thereafter to avoid possible chromatic aberrations due to its broad bandwidth. The pump, therefore, was tailored to match the signal. The pump beam implemented a telescope of two achromatic lenses, the spacing of which had fine adjustment. The pump and signal beams were focused into a PPLN crystal using a 40-mm focal length achromatic

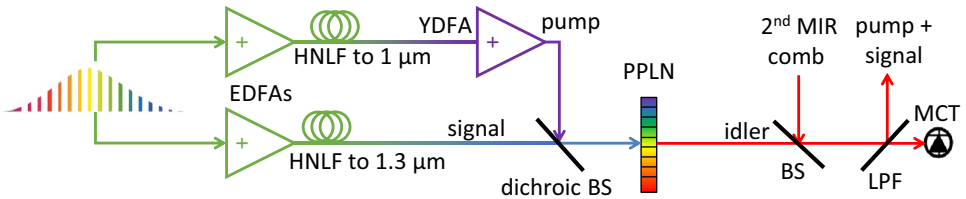

Fig. 2 Schematic of one of the two difference frequency generation (DFG) apparatuses. An erbium fiber oscillator was split into two branches. The pump branch (*top*) was amplified in an erbium-doped fiber amplifier (EDFA) before launching into highly nonlinear fiber (HNLF) to broaden the spectrum to 1 μm. This served as the seed for a ytterbium-doped fiber amplifier (YDFA). The signal branch (*bottom*) was also amplified in an EDFA and launched into a HNLF of different dispersion to broaden the spectrum to 1.3 μm. The output of these two branches were combined using a dichroic beam-splitter (BS), focused into to a periodically poled lithium niobate (PPLN) crystal. This generated idler spectra spanning 2.6–5.2 μm, the center wavelength of which was adjusted by choosing different poling periods. The generated mid-infrared light was combined with a second DFG system for dual-comb interferometry, and a long-pass filter (LPF) filtered out the pump and signal beams for diagnostic purposes and to isolate the idlers, which were detected on a mercury cadmium telluride (MCT) detector

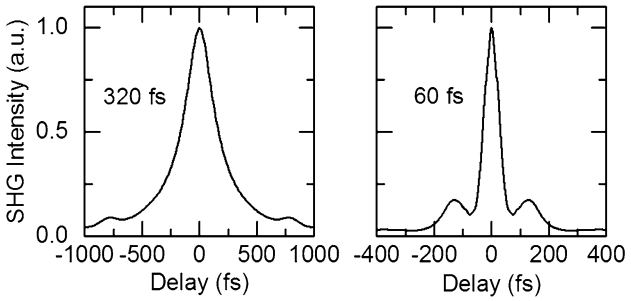

Fig. 3 Second harmonic generation autocorrelation of the 1-μm pump beam (*left*) and 1.3-μm signal beam (*right*). Delay vs. second harmonic intensity is plotted, and the autocorrelation width of each is shown adjacent to the plot

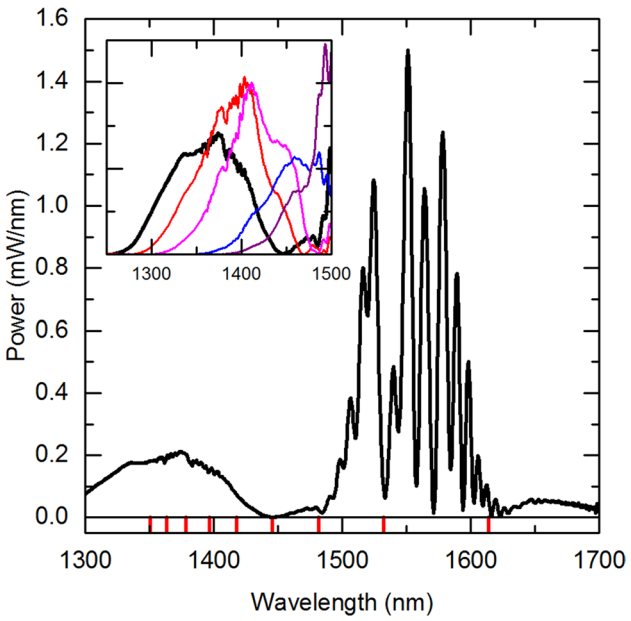

Fig. 4 Main figure: the broadened output of the EDFA used as the signal in the DFG process is shown in (*black*, *thick*). This spectrum was measured using a grating-based optical spectrum analyzer (OSA). The phase-matching wavelengths for different poling periods present in the PPLN crystal for a fixed 1074-nm pump are also indicated (*red*, *short sticks*). *Inset* The signal spectrum can be tailored for maximum signal power at a given poling period phase-matching wavelength by varying the pump current (original spectrum in *black*, *thick*; other spectra are *thin* and in *color*)

lens, and the telescope in the pump branch was adjusted so the two beams focused to the same plane. The beam waists of the pump and signal beams were 15 and 19 μm, respectively, measured using integrated power measurements with a translation stage and a razor blade. These correspond to average intensities of 200 kW/cm^2 for the pump and 15 kW/cm^2 for the signal. The PPLN crystal was either 1 or 3 mm in length, with poling periods that allowed for the quasi phase matching of 1 and 1.3–1.5 μm pump-signal pairs. The resulting output spectra, powers, and other characteristics are described in detail in later sections.

3.2 Pump and signal characterization

Maximal pulse compression is essential for optimal DFG in order to obtain the most peak power that drives the nonlinear process. The pump pulse duration was optimized using a free-space grating compressor, and the signal pulse duration was optimized via compression in polarization-maintaining, anomalous-dispersion, single-mode fiber before launching into PM HNLF. Second harmonic generation autocorrelations of both the pump and the 1.3–1.4 μm portion of the signal are shown in Fig. 3 at left and right, respectively. The autocorrelation widths of the pump and signal were 320 and 60 fs, respectively. If hyperbolic secant (sech^2) pulses are assumed, these correspond to minimum pulse durations of 210 and 40 fs. While clear evidence of incomplete compression is seen in the wings of these autocorrelations, the achievable pulse durations were not limiting factors in the subsequent DFG generation.

The spectrum of the signal used in 5-μm generation is shown in Fig. 4 in black, and the corresponding poling periods' phase-matching wavelengths for a 1074-nm pump are shown as short red sticks along the wavelength x-axis. The poling periods corresponding to the longest idler wavelengths correspond to the shortest signal wavelengths. The poling periods are (from left to right in Fig. 4): $\Lambda = 24.63$, 25.23, 25.86, 26.53, 27.22, 27.96, 28.74, 29.56, 30.43, and 31.35 μm (off-scale right). This spectrum was tailored specifically to generate optical power at the shortest phase-matchable signal wavelengths in order to generate long-wavelength idlers. However, the spectral peak between 1.3 and 1.4 μm can be moved to the red by reducing the pump power feeding the EDFA. These changes are shown in the inset in Fig. 4 as the thinner, colored lines, and these spectral choices allow for more efficient production of idler power between 3.5 and 4.5 μm.

4 Results and analysis

4.1 Spectral coverage

The attainable MIR spectral coverage using both 1 and 3 mm PPLN crystals was measured using a Fourier transform spectrometer, and is shown in Fig. 5. A fixed pump and signal were able to produce a tunable octave from 2.6–5.2 μm by simply changing the poling period of the PPLN crystal. Finer tuning can be achieved by changing the temperature of the PPLN crystal. The long-wavelength limit of the spectra shown is a result of the transparency window of PPLN; published values indicate that the absorption increases from

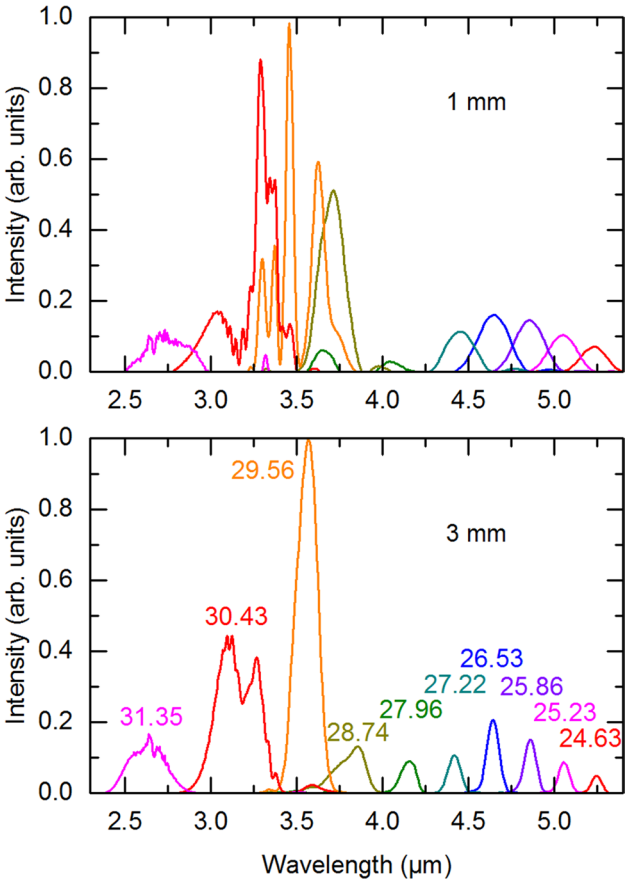

Fig. 5 The attainable spectral coverage using both 1 mm (*top*) and 3 mm (*bottom*) PPLN crystals. Spectra are scaled according to their measured integrated power. Each *colored* curve corresponds to a different poling period, shown in *color-coded text* (in microns) on the *bottom* plot. The gap seen near 4.2 μm results from weak power at the corresponding signal wavelength, as seen in Fig. 4. The longer of the two crystals has a narrower phase-matching bandwidth, and thus the spectra shown at *bottom* are narrower

roughly 10^{-2} cm^{-1} at 3 μm to 10^{-1} cm^{-1} at 4 μm and 1 cm^{-1} at 5 μm [53]. The peaks here are normalized to the measured integrated power (plotted in Fig. 7) and normalized to the maximum peak in each set. The spectral shapes are verified via simulation and explained in greater detail in Sect. 4.4. The spectra are suppressed at 4.2 μm in part due to weak signal power, but also as a result of the strong ro-vibrational absorption in ambient carbon dioxide in the path between the PPLN and the spectrometer used for characterization.

4.2 Beam characterization

One useful metric for determining the suitability of a laser beam for heterodyne detection, collimation, and both fiber and waveguide coupling is its mode quality. To our knowledge, beam quality from a DFG system in the 5-μm region has not been previously reported. We were able to evaluate this by collimating the 5-μm idler from one of the DFG systems, propagating it 2 m, then imaging it on an indium antimonide (InSb) camera array, shown in Fig. 6. Each axis of the beam profile was integrated and fitted with a Gaussian, shown in the axes above and to the right of the camera image. While the beam profile more closely resembles a Lorentzian, with more power in the wings than in a Gaussian, good modal quality is demonstrated and aids the heterodyne detection described in Sect. 4.5. The full-width at

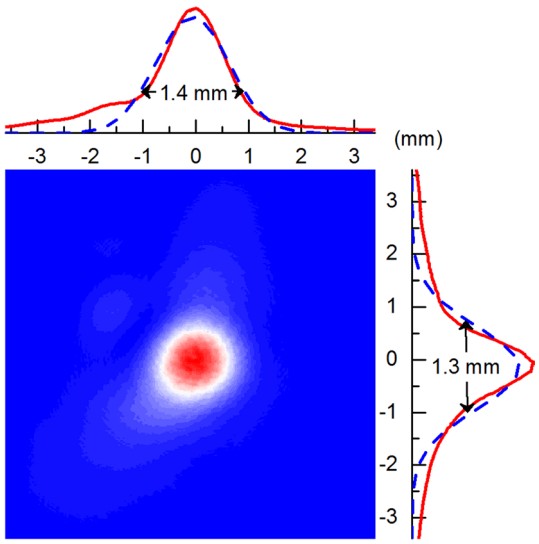

Fig. 6 Indium antimonide (InSb) camera image of collimated 5-μm beam, with line plots above and to the right showing the integrated *x*- and *y*-axes (*solid red*) and Gaussian fits to each (*dashed blue*)

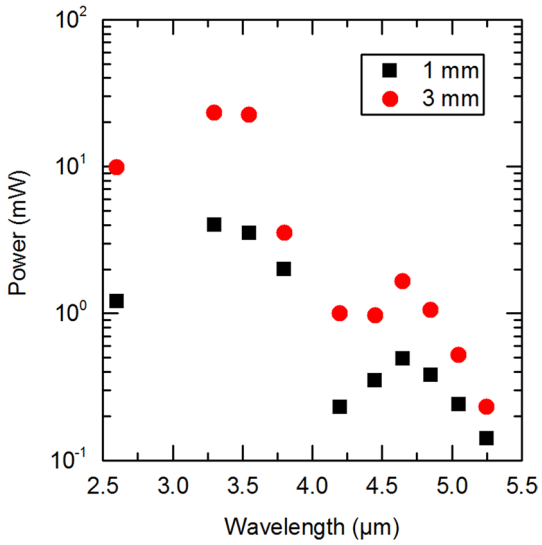

Fig. 7 Optical power as a function of wavelength for 1 mm (*black square*) and 3 mm (*red circle*) PPLN crystals, plotted on a logarithmic scale

half-maximum (FWHM) of the beam in the x-direction is 1.4 mm, and 1.3 mm in the y-direction.

4.3 Power measurements

DFG produced powers over a wide band of wavelengths ranging from roughly 100 μW (1 mm crystal, 5.2 μm) to over 20 mW (3 mm crystal, 3.5 μm). Powers using a 40-mm achromatic lens to focus beams into the crystal are plotted in Fig. 7. The focusing, alignment, and delay between the two input pulses were optimized for the 5.05-μm points; all other data points were taken after changing only the poling period and optimizing the delay. These were measured using a thermal power meter. At 5.05 μm, this 40-mm lens generated 280 μW in a 1-mm crystal and 520 μW in a 3-mm crystal. Powers were also measured at this wavelength using a 100-mm lens to focus; this yielded 175 μW in a 1-mm crystal, 860 μW in a 3 mm-crystal, and 1.37 mW in a 10-mm crystal. In the 1-mm crystal, the reduction in power is attributed to a larger beam waist, and thus lower input intensities. In the 3-mm crystal, the increase in power is attributed to the longer confocal parameter, which keeps the intensity more uniform throughout the crystal than the 40-mm lens. In fact, the 100-mm lens produces a confocal parameter of 92 mm, which is comparable to the 10-mm crystal length. This assures that the simulated powers, which did not account for beam diffraction, should approximate the experimental values well. Further gains can be achieved by increasing the pump power at 1 μm, optimized beam focusing at the crystal, and more careful tailoring of the broadened signal spectrum. (In a similar system, 0.5 W was achieved at 3 μm [33].)

Extensive numerical simulations were performed in an effort to verify the observed 5-μm idler power. In these simulations we find strong sensitivity to exact parameters of pump and signal intensity and relative overlap, which are challenging to precisely realize in the experiments. However, our model systematically predicted higher powers than were observed at the longest idler wavelengths. The source of this discrepancy is not known, but would be explained by stronger mid-infrared material absorption than what is expected for PPLN [53]. The possibility of nonlinear or multiphoton loss [61] due to the generation of parasitic green light was not explored. We note that reduced power at longer idler wavelengths was also observed in our earlier work [21]. Despite the lower than expected powers, the 5-μm light should be sufficient for lab spectroscopy, as detailed below.

4.4 Comparison to simulations

The spectral profile of the generated idler from this experiment was modeled and verified through numerical simulation. Figure 8 confirms the bandwidth of the idler in each crystal and poling period, from Fig. 5. The observed data points are shown as solid circles. These are not plotted as the full-width at half-maximum of the measured spectra directly, but divided by the convolution between the input pump and signal spectra to correct for some of the unusual spectral features found in the signal spectrum. (See the top panel of Fig. 5 between 3–4 μm for examples of idler spectral distortion.) Simulated bandwidths using Gaussian inputs are shown as solid lines, and, where the convolution correction is able to accurately recover a spectral shape, these agree quite well. At shorter wavelengths, the mid-infrared spectral width is limited by the spectral width of the signal (short dashes, horizontal line); at longer wavelengths, the mid-infrared spectral width is limited by the phase-matching bandwidth of PPLN (long dashes, plotted for a 1-mm crystal).

As can be seen from Fig. 8, the spectral bandwidth of the MIR comb, particularly at longer wavelengths, decreases as function of the crystal length. This is due to a corresponding decrease in the phase-matching bandwidth, which our model predicts well. The same model allows us to also predict the MIR pulse durations. For example, the pulse durations for the two cases of $z = 1$ mm and $z = 3$ mm are approximately 250 and 450 fs, respectively. The pulses are slightly chirped due to the group velocity mismatch in PPLN, which makes the pump and signal pulses travel faster than the idler. The modeling shows that the idler pulse is continuously generated as it walks away from the pump and signal, leading to an asymmetric time duration.

4.5 Coherence and noise measurements

With the source power and spectrum now evaluated, we are in the position to study the properties of this MIR DFG source for dual-comb spectroscopy. This was assessed by performing multi-heterodyne measurements between the two combs. Interferograms of the combined MIR combs were recorded using a high-bandwidth (>100 MHz) liquid nitrogen-cooled mercury cadmium telluride (MCT) detector. A sample interferogram from the overlapping of the two 5-μm combs is shown in Fig. 9, along with the resulting transformed spectra. Here, the two combs' repetition rates were roughly 99.84 MHz, with a repetition rate difference of 290 Hz. The interferogram is a single shot, unaveraged, with both combs free-running and without any active stabilization. The inset shows the resulting spectrum from one unaveraged interferogram, and the noise reduction of 16 interferogram averages. The time-domain signal-to-noise ratio of the interferogram is estimated to be approximately 25, within the 50 MHz Nyquist filtered bandwidth of the digital sampling system. With a repetition rate difference of 290 Hz,

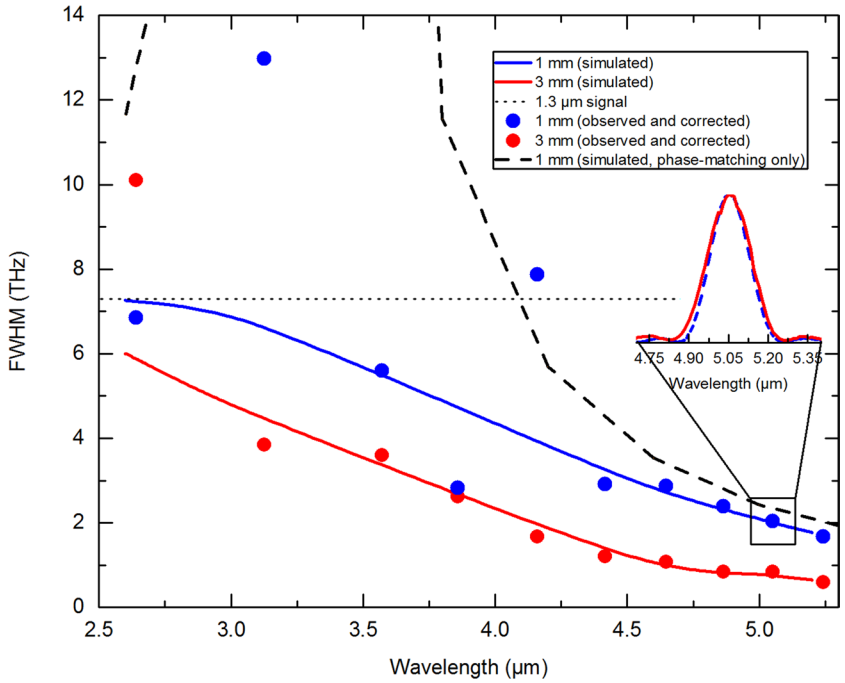

Fig. 8 Simulated and observed bandwidth in 1 and 3 mm PPLN crystals. *Dots* signify the corrected observed full-width at half-maximum (FWHM) measurements for the two different crystal lengths. The correction divides the observed FWHMs by the convolution of the input pump and signal, which allows for the removal of the effect signal's spectral features. The *solid lines* show the simulated bandwidth of the idler, assuming a Gaussian pump and signal of durations as determined via the autocorrelations shown in Fig. 3. *Dashed lines* show the bandwidth of the input signal and the phase-matching bandwidth of a 1-mm crystal solely via ΔkL walk-off. *Inset* simulated (*dashed*, *blue*) and experimental (*solid*, *red*) spectral widths for the 5.05-μm poling period

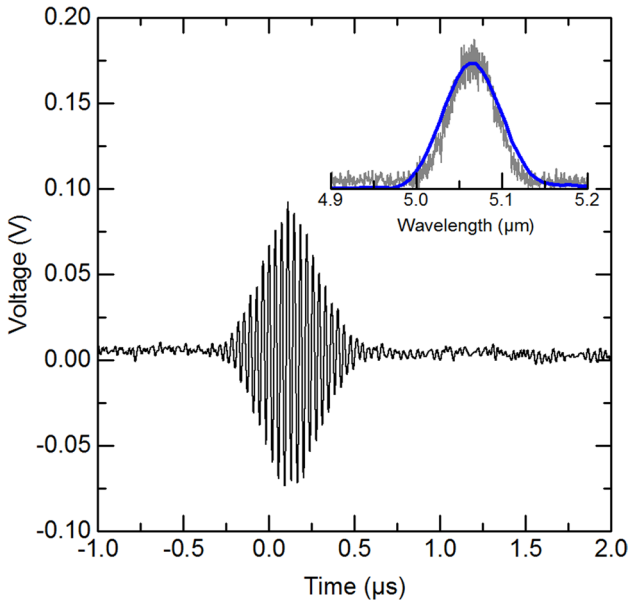

Fig. 9 Main figure: interferogram of free-running (unstabilized) 5-μm multi-heterodyne. *Inset* Fourier transform, re-scaled, of unaveraged interferogram (*gray*) and 16 averaged interferograms (*blue*)

interferograms occur every 3.4 ms. The averaging of 16 of these in succession, without stabilization or correction, demonstrates that the two mid-infrared combs exhibit coherence over at least 55 ms.

The relative intensity noise (RIN) was measured by analyzing the baseband voltage fluctuations on the average MIR power as detected with the MCT detector. Results are shown in Fig. 10. Electronic noise is seen at low frequencies, but is native to the measurement setup and not the MIR source or the MCT detector, as indicated by the electronic background. One can see that the mid-infrared RIN is greater than that of the pump and the signal, having acquired RIN from the pump. This is most evident at 10^4 Hz, where a peak is visible in both plots.

The mid-infrared RIN plotted here is not significantly higher than that typical of near-infrared fiber sources; depending on amplification, detector noise, dynamic range, and spectral broadening, RIN from an erbium-based fiber laser can range from −145 to −125 dBc/Hz [62]. Additionally, previous work using HNLF to broaden EDFA light from 1.5 to 2 μm produces comparable RIN to what is shown here [63].

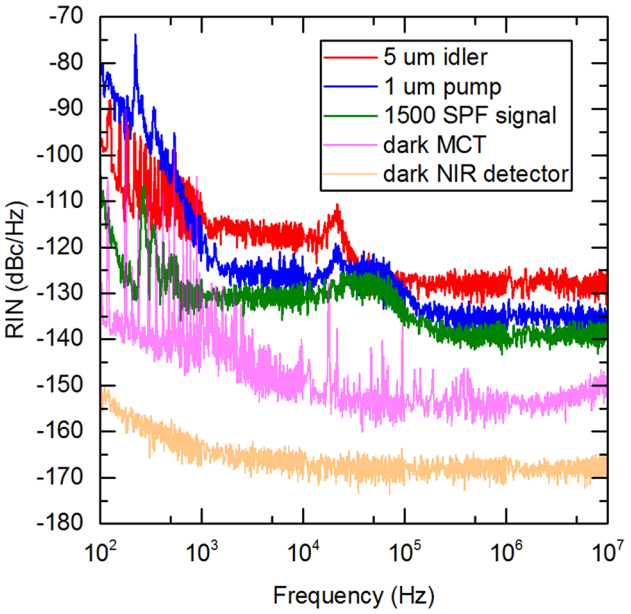

Fig. 10 The relative intensity noise (RIN) of the 1-μm pump, broadened portion of the 1.5-μm signal after passing through a 1500-nm short pass filter (SPF), the generated 5-μm idler, and both the near-infrared and mid-infrared detector backgrounds

5 Conclusions

Two 100-MHz optical frequency combs based on difference frequency generation were developed, with tunable spectral coverage ranging 2.6–5.2 μm. The use of polarization-maintaining fiber and a single-pass nonlinear process provides a path towards a reliable, stable source with the ability to cover a broad spectral region of great interest in molecular spectroscopy. In particular, the strong coherence and low RIN of this system show potential for immediate implementation in robust, high-sensitivity mid-infrared dual-comb molecular spectroscopy. The spectral shapes observed were explained and understood through numerical simulation. This particular system is limited by the transmission of PPLN, but a similar scheme implementing a more transmissive nonlinear crystal at longer wavelengths would allow for much broader tunability and access to new spectral regions.

Acknowledgements The authors thank Nathan Newbury and Ian Coddington of NIST for discussions, and Dan Hickstein and Kevin Cossel of NIST for useful feedback on the manuscript. We acknowledge the support of NIST (including the Greenhouse Gas and Climate Science Measurement Program), the DARPA SCOUT program, and CNPq (Brazil). This work is a contribution of the US Government and is not subject to copyright in the United States. The mentioning of company and product names is for technical communication only and does not constitute an endorsement by NIST.

References

1. A. Schliesser, N. Picqué, T.W. Hänsch, Nat. Phot. **6**(7), 440 (2012)
2. B.J. Bjork, T.Q. Bui, O.H. Heckl, P.B. Changala, B. Spaun, P. Heu, D. Follman, C. Deutsch, G.D. Cole, M. Aspelmeyer et al., Science **354**(6311), 444 (2016)
3. A.J. Fleisher, B.J. Bjork, T.Q. Bui, K.C. Cossel, M. Okumura, J. Ye, J. Phys. Chem. Lett. **5**(13), 2241 (2014)
4. I. Galli, S. Bartalini, S. Borri, P. Cancio, D. Mazzotti, P. De Natale, G. Giusfredi, Phys. Rev. Lett. **107**, 270802 (2011)
5. F. Tittel, D. Richter, A. Fried, in *Solid-State Mid-Infrared Laser Sources*, vol. 89, ed. by I.T. Sorokina, K.L. Vodopyanov. Topics in Applied Physics (Springer, Heidelberg, 2003), pp. 445–516. doi:10.1007/3-540-36491-9
6. P. Weibring, D. Richter, J.G. Walega, A. Fried, Opt. Express **15**(21), 13476 (2007)
7. K.C. Cossel, E.M. Waxman, I.A. Finneran, G.A. Blake, J. Ye, N.R. Newbury, JOSA B **34**(1), 104 (2017)
8. A. Dax, J.S. Wells, L. Hollberg, A.G. Maki, W. Urban, J. Mol. Spec. **168**(2), 416 (1994)
9. M. Mürtz, M. Schaefer, T. George, J. Wells, W. Urban, Appl. Phys. B **60**(1), 31 (1995)
10. M. Mürtz, J. Wells, L. Hollberg, T. Zibrova, N. Mackie, Appl. Phys. B **66**(3), 277 (1998)
11. V.O. Smolski, S. Vasilyev, P.G. Schunemann, S.B. Mirov, K.L. Vodopyanov, Opt. Lett. **40**(12), 2906 (2015)
12. F. Adler, K.C. Cossel, M.J. Thorpe, I. Hartl, M.E. Fermann, J. Ye, Opt. Lett. **34**(9), 1330 (2009)
13. K. Balskus, Z. Zhang, R.A. McCracken, D.T. Reid, Opt. Lett. **40**(17), 4178 (2015)
14. Z. Zhang, T. Gardiner, D.T. Reid, Opt. Lett. **38**(16), 3148 (2013)
15. A. Spott, J. Peters, M.L. Davenport, E.J. Stanton, C.D. Merritt, W.W. Bewley, I. Vurgaftman, C.S. Kim, J.R. Meyer, J. Kirch, L.J. Mawst, D. Botez, J.E. Bowers, Optica **3**(5), 545 (2016)
16. G. Villares, A. Hugi, S. Blaser, J. Faist, Nat. Commun. **5**, 5192 (2014)
17. Y. Yao, A.J. Hoffman, C.F. Gmachl, Nat. Phot. **6**(7), 432 (2012)
18. R.F. Curl, F. Capasso, C. Gmachl, A.A. Kosterev, B. McManus, R. Lewicki, M. Pusharsky, G. Wysocki, F.K. Tittel, Chem. Phys. Lett. **487**(1), 1 (2010)
19. F. Capasso, Opt. Eng. **49**(11), 111102 (2010)
20. C. Erny, K. Moutzouris, J. Biegert, D. Kühlke, F. Adler, A. Leitenstorfer, U. Keller, Opt. Lett. **32**(9), 1138 (2007)
21. T.W. Neely, T.A. Johnson, S.A. Diddams, Opt. Lett. **36**(20), 4020 (2011)
22. M. Tsuzuki, L. Jin, M. Yamanaka, V. Sonnenchein, H. Tomita, A. Sato, T. Ohara, Y. Sakakibara, E. Omoda, H. Kataura et al., Photonics Res. **4**(6), 313 (2016)
23. S.A. Meek, A. Poisson, G. Guelachvili, T.W. Hänsch, N. Picqué, Appl. Phys. B **114**(4), 573 (2014)
24. L.C. Sinclair, I. Coddington, W.C. Swann, G.B. Rieker, A. Hati, K. Iwakuni, N.R. Newbury, Opt. Express **22**(6), 6996 (2014)
25. M. Lezius, T. Wilken, C. Deutsch, M. Giunta, O. Mandel, A. Thaller, V. Schkolnik, M. Schiemangk, A. Dinkelaker, A. Kohfeldt et al., Optica **3**(12), 1381 (2016)
26. A. Gambetta, D. Gatti, A. Castrillo, G. Galzerano, P. Laporta, L. Gianfrani, M. Marangoni, Appl. Phys. Lett. **99**(25), 251107 (2011)
27. K.C. Cossel, F. Adler, K.A. Bertness, M.J. Thorpe, J. Feng, M.W. Raynor, J. Ye, Appl. Phys. B **100**(4), 917 (2010)
28. M.J. Thorpe, D. Balslev-Clausen, M.S. Kirchner, J. Ye, Opt. Express **16**(4), 2387 (2008)

29. G.B. Rieker, F.R. Giorgetta, W.C. Swann, J. Kofler, A.M. Zolot, L.C. Sinclair, E. Baumann, C. Cromer, G. Petron, C. Sweeney, P.P. Tans, I. Coddington, N.R. Newbury, Optica **1**(5), 290 (2014)
30. F. Keilmann, C. Gohle, R. Holzwarth, Opt. Lett. **29**(13), 1542 (2004)
31. I. Coddington, N. Newbury, W. Swann, Optica **3**(4), 414 (2016)
32. F. Zhu, A. Bicer, R. Askar, J. Bounds, A. Kolomenskii, V. Kelessides, M. Amani, H. Schuessler, Laser Phys. Lett. **12**(9), 095701 (2015)
33. F.C. Cruz, D.L. Maser, T. Johnson, G. Ycas, A. Klose, F.R. Giorgetta, I. Coddington, S.A. Diddams, Opt. Express **23**(20), 26814 (2015)
34. M. Yu, Y. Okawachi, A.G. Griffith, N. Picqué, M. Lipson, A.L. Gaeta, arXiv preprint arXiv:1610.01121 (2016)
35. M. Yan, P.L. Luo, K. Iwakuni, G. Millot, T.W. Hänsch, N. Picqué, arXiv preprint arXiv:1608.08013 (2016)
36. Y. Jin, S.M. Cristescu, F.J. Harren, J. Mandon, Appl. Phys. B **119**(1), 65 (2015)
37. B. Bernhardt, E. Sorokin, P. Jacquet, R. Thon, T. Becker, I. Sorokina, N. Picqué, T. Hänsch, Appl. Phys. B **100**(1), 3 (2010)
38. V.O. Smolski, H. Yang, J. Xu, K.L. Vodopyanov, arXiv preprint arXiv:1608.07318 (2016)
39. E. Baumann, F.R. Giorgetta, W.C. Swann, A.M. Zolot, I. Coddington, N.R. Newbury, Phys. Rev. A **84**, 062513 (2011)
40. A. Gambetta, N. Coluccelli, M. Cassinerio, D. Gatti, P. Laporta, G. Galzerano, M. Marangoni, Opt. Lett. **38**(7), 1155 (2013)
41. A. Gambetta, R. Ramponi, M. Marangoni, Opt. Lett. **33**(22), 2671 (2008)
42. A. Ruehl, A. Gambetta, I. Hartl, M.E. Fermann, K.S.E. Eikema, M. Marangoni, Opt. Lett. **37**(12), 2232 (2012)
43. Y. Yao, W.H. Knox, Opt. Express **21**(22), 26612 (2013)
44. L. Nugent-Glandorf, F.R. Giorgetta, S.A. Diddams, Appl. Phys. B **119**(2), 327 (2015)
45. F. Zhu, H. Hundertmark, A.A. Kolomenskii, J. Strohaber, R. Holzwarth, H.A. Schuessler, Opt. Lett. **38**(13), 2360 (2013)
46. F. Keilmann, S. Amarie, J. Infrared Millim. Terahertz Waves **33**(5), 479 (2012)
47. L. Jin, M. Yamanaka, V. Sonnenschein, H. Tomita, T. Iguchi, A. Sato, T. Oh-hara, N. Nishizawa, Appl. Phys. Express **10**(1), 012503 (2016)
48. I. Galli, F. Cappelli, P. Cancio, G. Giusfredi, D. Mazzotti, S. Bartalini, P. De Natale, Opt. Express **21**(23), 28877 (2013)
49. I. Galli, S. Bartalini, P. Cancio, F. Cappelli, G. Giusfredi, D. Mazzotti, N. Akikusa, M. Yamanishi, P. De Natale, Opt. Lett. **39**(17), 5050 (2014)
50. K. Iwakuni, S. Okubo, O. Tadanaga, H. Inaba, A. Onae, F.L. Hong, H. Sasada, Opt. Lett. **41**(17), 3980 (2016)
51. A. Sell, G. Krauss, R. Scheu, R. Huber, A. Leitenstorfer, Opt. Express **17**(2), 1070 (2009)
52. D.S. Hum, M.M. Fejer, Comptes Rendus Physique **8**(2), 180 (2007)
53. M. Leidinger, S. Fieberg, N. Waasem, F. Kühnemann, K. Buse, I. Breunig, Opt. Express **23**(17), 21690 (2015)
54. J.C. Diels, W. Rudolph, *Ultrashort Laser Pulse Phenomena, Second Edition (Optics and Photonics Series)*, ed. by P.F. Liao, P. Kelley (Academic Press, Burlington, MA, 2006)
55. S. Witte, R. Zinkstok, W. Hogervorst, K. Eikema, Appl. Phys. B **87**(4), 677 (2007)
56. I.N. Ross, P. Matousek, G.H.C. New, K. Osvay, JOSA B **19**(12), 2945 (2002)
57. J. Seres, J. Hebling, JOSA B **17**(5), 741 (2000)
58. F. Quinlan, T.M. Fortier, M.S. Kirchner, J.A. Taylor, M.J. Thorpe, N. Lemke, A.D. Ludlow, Y. Jiang, S.A. Diddams, Opt. Lett. **36**(16), 3260 (2011)
59. G. Ycas, S. Osterman, S.A. Diddams, Opt. Lett. **37**(12), 2199 (2012)
60. G. Krauss, S. Lohss, T. Hanke, A. Sell, S. Eggert, R. Huber, A. Leitenstorfer, Nat. Phot. **4**(1), 33 (2010)
61. H. Mabuchi, E. Poizik, H.J. Kimble, JOSA B **11**(10), 2023 (1994)
62. N.R. Newbury, I. Coddington, W. Swann, Opt. Express **18**(8), 7929 (2010)
63. A. Klose, G. Ycas, D.L. Maser, S.A. Diddams, Opt. Express **22**(23), 28400 (2014)